Full-field analysis of damage under complex thermomechanical loading

Nicolas Leost, Alain Köster, Djamel Missoum-Benziane, Matthieu Rambaudon, Laurent Cameriano, François Comte, Brice Le Pannerer, Vincent Maurel

Full-field analysis of damage under complex thermomechanical loading

Nicolas LEOST[a,b], Alain KÖSTER[a], Djamel MISSOUM-BENZIANE[a], Matthieu RAMBAUDON[a], Laurent CAMERIANO[b], François COMTE[b], Brice LE PANNERER[b], Vincent MAUREL[a]

[a]*Mines Paris, PSL University, Centre for material sciences (MAT), UMR7633 CNRS, 91003 Evry, France*
[b]*Safran Aircraft Engines Villaroche, Rond-Point René Ravaud, 77550 Moissy-Cramayel, France*

Abstract

This study combines infrared thermography, digital image correlation and machine learning to measure respectively temperature, strain and damage fields at high temperature. This is applied to thermomechanical fatigue (TMF) testing in presence of severe gradient for typical out-of-phase loading condition. This type of loading is challenging when dealing with thin sheets due to buckling risk induced by high temperature compression. For a Co-based superalloy (Haynes 188), this study demonstrates full-field identification/validation of both behavior and damage models. Thermal gradient model is the key point in this analysis. With the coupling of TMF measurements by machine learning and DIC, local fatigue micro-crack growth rate and localisation are assessed through jump in displacement. TMF finite element analysis, of loading and damage, validates the whole model framework.

Keywords: Thermomechanical fatigue (TMF), Crack detection, Digital image correlation (DIC), Machine learning (ML), Haynes 188 (Ha188)

Contents

*Corresponding author
Email address: nicolas.leost@minesparis.psl.eu (Nicolas LEOST)

1. Introduction

Combination of digital image correlation (DIC) technique with infra-red thermography (IRT), the so-called hybrid view technique, is straightforward to assess damage in rather low temperature context [1, 2, 3, 4]. It has been recently developed for measuring in situ both strain fields, by DIC, temperature gradients, by IRT, and damage by direct image analysis and DIC results up to 600 °C [5]. The limitation in temperature is associated to several factors standard for image acquisition: blur induced by hot gas flux, saturation of CCD by illuminance and material oxidation [6]. To overcome these difficulties, several options exist in literature to reach temperatures above 1200 °C at the cost of a complex experimental set-up [7, 8, 9, 10, 11]. Moreover, although some authors use incidental microstructure or details provided by oxidation [12, 13, 14], high temperature DIC methods usually require a speckling technique that should stand for high temperature when oxidation evolves quickly. Pattern speckle processing has been the object of intensive work these last years [15], and a recently developed LASER-engraved speckling is found to be a robust candidate to enable a full-field acquisition at high temperature [16, 17]. Although DIC aims to assess strain fields, measured displacements fields may be used to detect crack initiation or crack path through the detection of DIC residues and/or discontinuous displacements [18, 19, 20, 14]. Adding machine learning (ML) to these techniques, offers new possibilities in terms of both spatial resolution and nature of the objects to be detected such as micro-cracks. ML is now widely used to automate the process of crack detection [21], e.g. it has already been performed in the context of road cracks [22, 23, 24].

This paper proposes an original combination of these techniques in the environment of severe thermo-mechanical fatigue (TMF) loading implying high temperature, oxidation, temperature gradient, mechanical and thermal cycling. Such conditions aim to mimic realistic loading beared by component exposed to high temperature for which study of damage mechanisms is a key point. Most studies dealing with these complex TMF conditions are achieved in the scope of either lifetime to failure analysis or long crack analysis. The former limits possibilities of clarification of damage mechanisms, yielding large scatter in lifetime assessment [25]. The latter are only suitable to describe fatigue crack growth in the long crack domain with very few analysis of gradient impact on the crack behavior. Among theses studies, the work proposed by Kim et al. is of high interest, but is addressing only limited level of temperature gradient, and no full-field analysis of impact of strain and damage gradients in fatigue crack growth rate [26].

The industrial application targeted in this study is combustion chambers for aeronautical engines made of superalloy thin sheets assembly. For typical TMF loading observed in these components, some critical points are subjected to out-of-phase (OP) loading where high temperature compression may induce buckling of thin sheets in lab experiment. However, literature data for this class of alloys (e.g. Ha188, Ha230, Hastelloy-X...) are mostly available for wrought or cast alloys. Besides, few data deals with TMF condition for the alloy of interest here, the Ha188, where most of them are related to lifetime analysis [27, 28]. This point pushes the need of in-depth study of fatigue crack growth, by the way lifetime in low cycle fatigue (LCF) condition is mostly governed by crack propagation. This has been analyzed for long crack in generalized plasticity but limited to isothermal condition in [29, 30]. For micro-crack propagation, original proposition was executed also in isothermal condition in [31]. Thus, it is a challenge to achieve OP-TMF test for thin sheet material together with a robust tracking of micro-crack growth to gain relevancy in testing condition as compared to industrial application.

To overcome these experimental difficulties, a test methodology using a coplanar biaxial fatigue device has been designed. For that purpose, combining a cross-shaped specimen and an inductor with concentric coils [32] allows to obtain both load control and a temperature gradient under thermal cycling. A such experimental environment is associated with high level of noise to signal ratio for image based analysis, the challenge being to describe damage mechanisms related to local loading conditions despite these difficulties. Besides, measurement of the fatigue crack growth rate with micro-cracks is challenging when dealing with high temperature condition for which oxidation impacts the possibilities of image based analysis.

The chosen original set-up to obtain OP-TMF cycling with gradient is first described together with experimental methods carried out for full-field analysis combining IRT, DIC and ML. To clarify the effect of OP-TMF loading, a comparison with micro-crack growth rate analyzed through isothermal testing will be achieved. These tests are thus also briefly introduced. Then FEA details are given to assess mechanical state for the chosen complex condition of OP-TMF in presence of gradient, for thermal and mechanical analysis. The first results to be detailed are the evolutions with time and full-field measurements of both temperature and mechanical strain. A first validation of FEA is thus proposed on this basis. The damage field is derived from ML performed on SEM images, and micro-crack growth rate is obtained through gradient analysis of displacement field measured in situ. Then validation of the experimental method is proposed by the comparison of FCGR for two similar testing OP-TMF conditions. Further comparison with isothermal micro-crack growth is detailed. This paves the way to FCGR base damage model and the final comparison of damage field reached in OP-TMF testing and assessed by this model. The final discussion aims at clarifying, in terms of spatial resolution, what are the gains of the proposed methodology, together with the new results obtained for Ha188 in OP-TMF loading.

2. Material and experimental methods

2.1. Material and specimen

The material used in this study is the Haynes 188 (Ha188) superalloy processed from hot-rolled thin sheet. The as-received thickness is e=1.5 mm. The alloy is solution heat-treated up to 1205 °C and rapidly air cooled. Its composition is detailed in Table 1 and its main mechanical and physical properties are summarized in Table 2.

Table 1: Chemical composition of the studied Ha188 superalloy (wt.%) [33].

Element	Co	Ni	Cr	W	Fe	Mn	Si	C	La	B
Weight%	39	22	22	14	3	1.25	0.35	0.10	0.03	0.015

A cross-shaped specimen was previously used for long crack analysis, but using a 3 mm thickness [32]. Derived from this design, a new specimen was machined with in its center a hole of 10 mm in diameter using the nominal thickness of the sheet in its as-received state of 1.5 mm. The central hole mimics a cooling hole for the combustion chamber where cracks are most likely to initiate. The entire specimen including the central hole was machined by milling, see Figure 1.

2.2. Experimental thermomechanical fatigue set-up and loading

Due to engine start and shut-down, and variation of flame during flight, combustion chambers cooling holes sustain low cycle fatigue (LCF) in presence of large variations of temperature in both time and space. These operating conditions are typical of TMF in presence of thermal and subsequent mechanical gradients. The following experimental design aims to be representative of the out-of-phase thermomechanical fatigue (OP-TMF) loadings in gradient conditions that the industrial part may sustain during its lifetime.

The set-up consists in a coplanar fatigue facility (Instron 8800), which is able to bear 100 kN on each of the four orthogonal actuators. At the center of the specimen, an inductor with concentric coils enables

Table 2: Physical and mechanical properties of the studied Ha188 superalloy [33]: Thermal Conductivity k, Thermal Diffusivity D, Mean Coefficient of Thermal Expansion α, Dynamic Modulus of Elasticity E, Poisson's Ratio ν and 0.2% Yield Strength $R_{p0.2}$ at room temperature (RT), 300 °C, 800 °C, 900 °C and 1000 °C.

T (°C)	k ($W.m^{-1}.°C^{-1}$)	D ($cm^2.s^{-1}$)	α ($°C^{-1}$)	E (GPa)	ν	$R_{p0.2}$ (MPa)
RT	10.4	$29.2\ 10^{-3}$	$\varnothing$	232	0.3	483
300	15.9	$38.7\ 10^{-3}$	$13.1\ 10^{-6}$	213	0.29	390
800	24.8	$50.4\ 10^{-3}$	$15.5\ 10^{-6}$	171	0.32	290
900	25.5	$50.4\ 10^{-3}$	$16.0\ 10^{-6}$	160	0.33	224
1000	27.6	$53.0\ 10^{-3}$	$16.5\ 10^{-6}$	150	0.33	120

Table 3: Cartesian and cylindrical coordinates of thermocouples (TCs) and pyrometer (Pyro) laser pointers for TMF1 and TMF2 tests: axes are defined in Figure 1(b), Z=0 corresponds to the side of the specimen observed in situ - Frontside, Z=-1.5 corresponds to the side of the specimen where inductor is located - Backside

Name	X (mm)	Y (mm)	Z (mm)	r (mm)	θ (°)
Pyro TMF1	-8	0	0	8	180
Pyro TMF2	-5	5	0	7	135
TC1	-17.5	17.5	-1.5	25	135
TC2	-10.5	10.5	-1.5	15	135
TC3	-19	0	0	19	180
TC4	0	19	0	19	90
TC5	19	0	0	19	0
TC6	0	-19	0	19	270
TC7	7	-7	-1.5	10	315
TC8	14	-14	-1.5	20	315

to heat the specimen. To improve the geometry of the inductor, in particular the space between coils, this inductor was processed by laser power bed fusion [32]. The temperature gradient being driven by the choice of the inductor geometry: the larger the diameter of the inductor, the lower the observed temperature gradient in the gage length of the cross-shaped specimen [32, 34]. Temperature control is

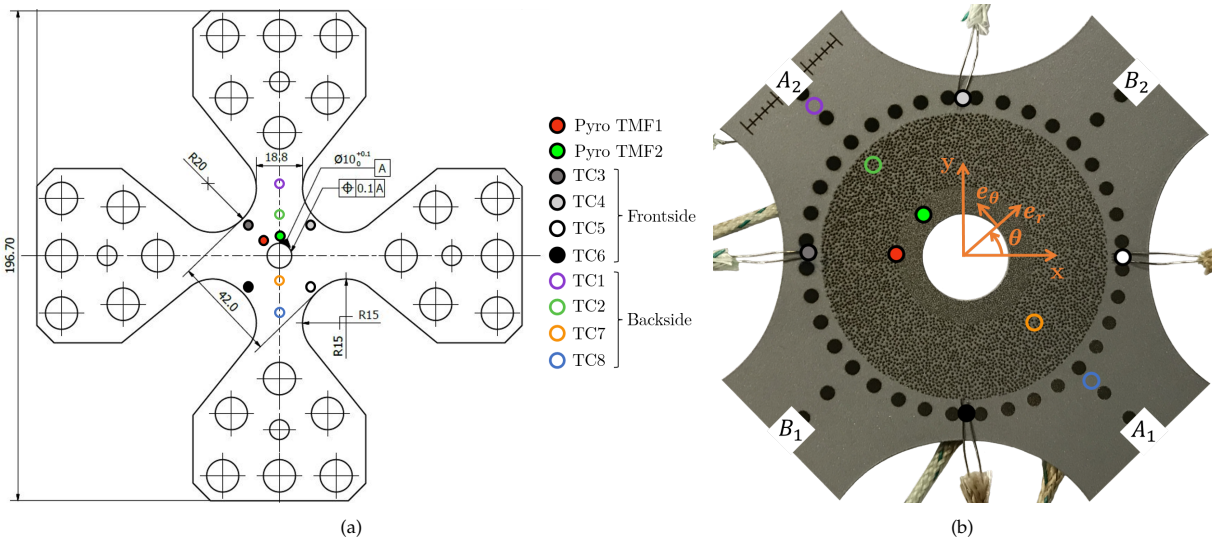

(a) (b)

Figure 1: Cross-shaped specimen with a 10 mm central hole: (a) Sketch of the specimen, colored labels correspond to thermocouples (TC) and pyrometer (Pyro) locations; (b) Front view of the specimen with the LASER-engraved speckling and markers (partial view).

Table 4: Testing conditions for OP-TMF loadings from this study and for isothermal LCF loadings from [31]; for OP-TMF the range of temperature is prescribed through the pyrometer

Name	Temperature	Loading	R_ε	Reference
TMF1	300-900 °C	u=0		This study
TMF2				
LCF1	900 °C	$\Delta\varepsilon$=0.15 %	0	[31]
LCF2		$\Delta\varepsilon$=0.20 %		
LCF3		$\Delta\varepsilon$=0.30 %		
LCF4		$\Delta\varepsilon$=0.50 %		
LCF5		$\Delta\varepsilon$=0.75 %		
LCF6		$\Delta\varepsilon$=1.50 %	-1	

associated to an infra-red pyrometer, monitored through a closed loop.

The thermal cycling is set to evolve from 300 to 900 °C, with a heating and cooling rates set to 300 and 150 °C/min respectively. During first heating, forces were controlled to zero. To obtain the targeted TMF condition, as soon as the maximum heating is reached for the first time, displacements were prescribed to zero on each of the four actuators (u=0 Table 4) defining the "0" cycle. This displacement constraint is kept all along the test, playing only on temperature variation with cycling as described above. These testing conditions favour an a priori OP-TMF loading at a global scale length: compression at high temperature and tension during low temperature steps respectively.

Based on this experimental set-up and loading, two similar testing conditions will be detailed in this study. The only difference to be considered is the location of the point to control temperature through pyrometer. This modification has a direct consequence on the temperature field, and especially on the local temperature reached where major crack has initiated. However, TMF conditions are otherwise very similar and thus comparable to each other. To precise the location of pyrometer and thermocouples, a cylindrical coordinate system will be used, see Figure 1(b). One test condition, referred as to TMF1 in the sequel (Pyro. TMF1 in Figure 1), corresponds to a temperature control point located 3 mm from the edge of the central hole toward the specimen fillet between A2 and B1, r=8 mm and θ=180°; the other test condition, referred as to TMF2 in the sequel (Pyro. TMF2 in Figure 1), corresponds to a temperature control point located 2 mm from the edge of the central hole toward the specimen arm A2, r=7 mm and θ=135°, see Figure 1 and Table 3 for pyrometer locations.

The whole method developed in this study will be detailed on the basis of TMF1 testing condition. Comparison between TMF1 and TMF2 will be discussed afterwards.

2.3. Experimental isothermal fatigue reference set-up and loading

On the other hand, looking for reference test in open literature, very few data are available for micro-crack growth for the studied material. Thus, to clarify the impact of TMF loading in both micro-crack propagation and lifetime, a test series executed in isothermal condition will be used for sake of comparison. This test series has been carefully detailed in previous works, the interested reader can refer to [31, 29].

To summarize, the testing conditions were as follows: the tested material was the same as studied in the present work, namely Ha188 machined from cast alloy, the whole test series was achieved at 900 °C (controlled by K-type thermocouple), under strain controlled conditions. The specimen was designed as a 20 mm long and 4 mm thick gage length, Figure 2. To achieve micro-crack growth analysis, three holes of 1 mm in diameter were processed by electro-discharge machining within the gage length (axis of the holes being orthogonal to the flat sides of the specimen and to the loading direction), see A-A view in Figure 2.

Last but not least, the high temperature extensometer, made of alumina rods, was used with an initial distance of 10 mm between rods contact points with the specimen; the rods being equally spaced around the central machined hole.

The different test conditions are summarised in Table 4.

2.4. Temperature field measurement by infrared thermography

Acquisition of temperature field is carried out using an infrared (IR) camera (Flir SC7000, 320x256 pixels, $\lambda \in [1.9 - 5.1\,\mu m]$) for a pixel resolution of 200 µm and with a frame rate of 1 frame per second. Moreover, local temperatures were measured using a pyrometer (IMPAC IPE 140, $\lambda \in [3.0 - 5.0\,\mu m]$) with an acquisition frequency of 100 Hz and eight chromel-alumel (Ni-Cr/Ni-Al) thermocouples (K-type) with an acquisition frequency of 10 Hz, see Figure 1 and Table 3 for the locations of the thermocouples (TCs) and pyrometer laser pointers (Pyro).

IR camera acquisition was executed sequentially for each step of 100 °C measured by the pyrometer during the thermal calibration pre-test, see thermal calibration set-up Figure 3(a) and (c), whereas pyrometer and thermocouples are used continuously during the thermal calibration and the mechanical testing. The sequential acquisition of the IR camera allowed to progressively adjust the thermal acquisition range during the heating. Emissivity of the specimen varies with oxidation. Thus, TCs are used as references to control the emissivity and to fit temperature field acquired by IRT camera to TCs values. Pyrometer value is modified so as to fit with local temperature measured by IRT. By regulating the temperature with a pyrometer on the hotspot, it is possible to avoid the welding of a thermocouple in the vicinity of the central hole, which could promote the initiation of cracks and disturb the displacement field measurements by DIC.

Temperature field provides informations about the temperature gradient induced by the induction heating, but also on the targeted off-centre heating at low and high temperatures. The pyrometer and the thermocouples, welded on both the front (cameras) and rear (inductor) sides of the specimen, allow respectively monitoring and measuring temperature during the test. IRT analysis were performed using Altair software and are exported into MATLAB software environment.

2.5. Strain field measurement by digital image correlation

Acquisition of local displacement fields is carried out by three synchronised cameras (Baumer VCXU-51C, 2448x2048 pixels) for a pixel resolution of 26 µm for camera 1 and 2 and 7.5 µm for camera 3, see experimental test set-up Figure 3(b) and (c). The three cameras are set to 1 frame every 8 seconds. Global displacement fields at the specimen scale is obtained by 3D stereo-correlation with the two peripheral cameras 1 and 2 [35, 36]. The stereo-correlation system was calibrated using a standard calibration target with 14x10 dots and a grid spacing of 3 mm. Local displacement fields, to get information at the crack length scale, is obtained by 2D correlation with camera 3 [37, 38]. All DIC analysis and calibration were performed using Vic-2D® and Vic-3D® software and are exported into MATLAB software environment.

LASER-engraved speckling and markers [16] make DIC possible insofar as they do not fade at high temperature and remain visible despite oxidation. The surface of the specimen was sandblasted using

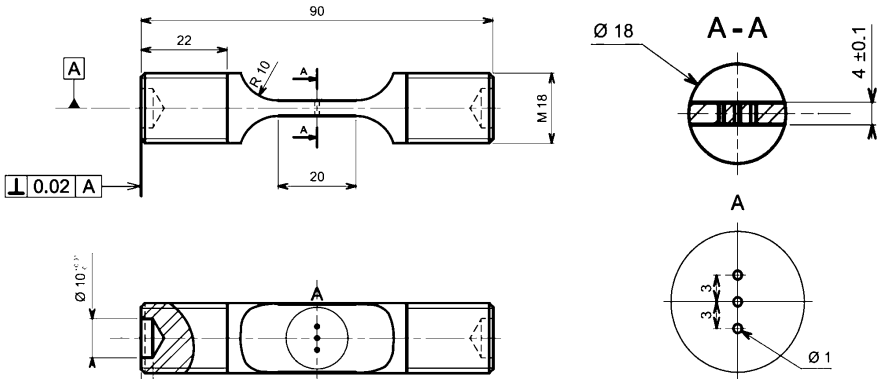

Figure 2: Sketch of the specimen used for isothermal testing [31, 29]

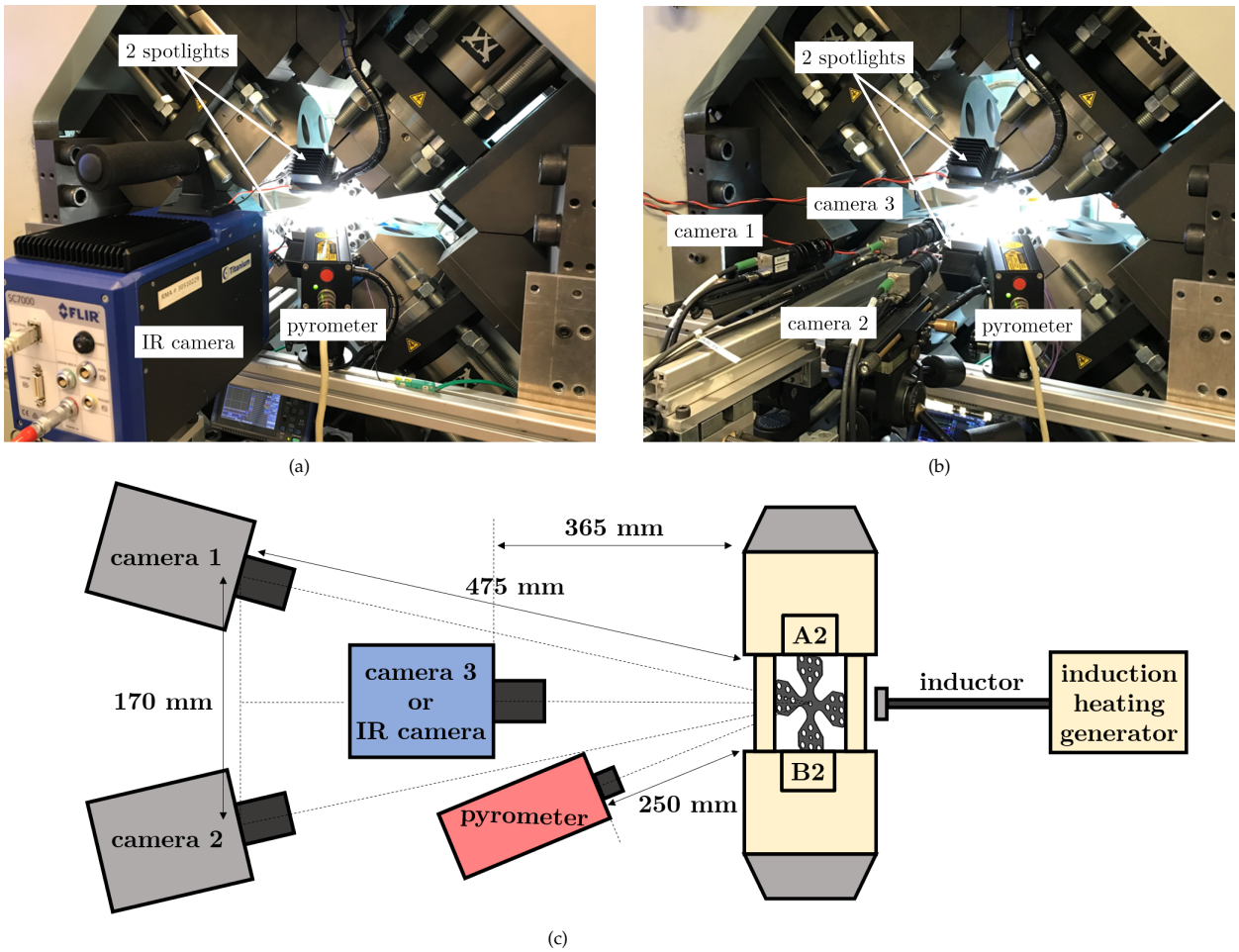

Figure 3: Experimental set-up detailing the front side where field acquisitions are performed; the inductor is on the other side of the facility: (a) Front view of the thermal calibration set-up before mechanical testing; (b) Front view of the three synchronised cameras set-up during mechanical testing; (c) Sketch of the top view of the experimental set-up.

glass beads to create a matt look to enhance the contrast with the speckles for better DIC results, Figure 1)(b). In addition, two spotlights illuminate the specimen, thus annihilate intense light radiation from the specimen at 900 °C and maintain a constant specimen illuminance during anisothermal cycles, Figure 3(b). The quality of DIC and its resolution are improved by a progressive speckling with three levels of density and size. The coarsest resolution is associated to markers of 1.5 mm in diameter, located each 10° of arc on a circle of 18 mm of radius, appearing as dark disk on Figure 1)(b). Used by pairs, they provide a multiaxial virtual extensometer. Markers tracking is performed using a python code developed at Centre for material sciences - Mines Paris.

For strain field measurement, a refined pattern was processed in an area delineated by two circles of 16.5 mm and 8 mm of radius respectively with speckles consisting in circles of 0.3 mm in diameter and a density of 7 patterns per mm², see variation of contrast in Figure 1)(b). The finest speckle was processed within a circle of 8 mm in radius, using LASER speckle of 0.1 mm and a density of 30 patterns per mm².

2.6. Micro-cracks field automated measurement by machine learning

Due to the similar grey level of the cracks and the speckles observed on scanning electron microscope (SEM) images, see Figure 4(a), a classical image segmentation cannot be performed systematically or will consist in an extremely time consuming task at the scale length of the whole specimen. Machine learning

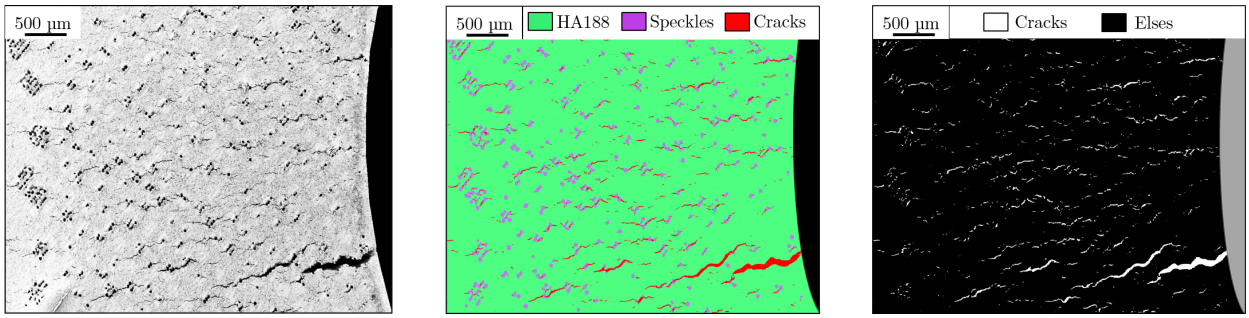

(a) (b) (c)

Figure 4: Training phase of images segmentation by ML: (a) SEM image; (b) Image segmentation results with three classes defined; (c) Image segmentation by ML binarised, cracks being associated to white color.

(ML) algorithms are sounded to classify objects based on their aspect ratio, and are thus straightforward to automatically identify a large number of cracks.

For image based analysis, such classification can be executed using the "Trainable Weka Segmentation" plugin included into the software ImageJ [39]. This ML segmentation is based on a supervised pixel classification by a random forest algorithm [40, 41, 24].

The "training" phase includes specification of the different "classes" that need to be detected by ML from an entry image (Figure 4(a)). As shown in Figure 4(b), three classes have been specified: the material Ha188, the speckles and the cracks. A distinct class was specified for the speckles because it should not be confused with micro-cracks, which could lead to an overestimation of damage. A final step consists in simple image segmentation to binarize images between the micro-cracks and other classes, see Figure 4(c). From this first image segmentation, called "training" phase, a model can be saved to performed other images segmentation with same classes learned by ML.

In order to evaluate, the quality of the trained ML model, a "test" phase is usually performed. This test consists in using the ML model previously trained on others images of the data set to be compared with "ground truth" images that is the ideal expected results for the same set of images. Thus, a "ground truth" image was created by identifying manually, as accurately as possible, all different classes "cracks", "Ha188" and "speckles". Then the trained model was used on this same image to predict pixels classification by ML. Precision and recall are two widely used performance metrics for ML classification that can be defined for each class [42, 43]. Precision of a class is the fraction of relevant pixels (true positive) among the predicted pixels, see equation 1, and recall is the fraction of relevant pixels that were predicted, see equation 2. In addition, accuracy performance metric attests the fraction of pixels predicted correctly (both true positive and true negative), see equation 3 .

$$precision = \frac{TP}{TP + FP} \tag{1}$$

$$recall = \frac{TP}{TP + FN} \tag{2}$$

$$accuracy = \frac{TP + TN}{TP + TN + FP + FN} \tag{3}$$

where TP, TN, FP and FN are true positives, true negatives, false positives and false negatives respectively. Finally, the f1-score conveys the balance between the precision and the recall and is defined as follows equation 4:

$$f1 - score = 2 \times \frac{precision \times recall}{precision + recall} \tag{4}$$

Table 5: Precision, recall and f1-score of the trained machine learning model for classes "Cracks", Ha188" and "Speckles" using scikit-learn python code [44].

	Precision	Recall	F1-score	Support
Cracks	0.64	0.70	0.67	4455
Ha188	1.00	0.99	0.99	513567
Speckles	0.66	0.90	0.76	13434
Accuracy			0.98	531456

Precision, recall and f1-score are calculated using a scikit-learn python code [44] and are displayed Table 5, "support" being the number of pixels for the "test" phase analysis.

The overall high accuracy score shows the good ratio between the correct predictions and the total number of pixels (support) evaluated. This is partly due to the high number of pixels associated to the "Ha188" class that were correctly detected. The quality of the model regarding crack detection is of lower quality, but the results are still very satisfactory with a recall score close to the precision score, see Table 5.

3. Finite element analysis of thermomechanical gradients

Finite elements analysis (FEA) was first carried out by a transient 3D thermal calculation. Then a full 3D mechanical FEA has been achieved accounting for elasto-viscoplastic (EVP) behavior function of the local temperature evolution together with thermal strain variations. All FEAs and post-processing calculations were performed using the Z-set software (version Z9.1.0) [45].

A mesh of quadratic tetrahedral elements with a mesh size of 1 mm in the region of interest was processed using the Gmsh software [46]. Each element is made of ten nodes and four Gauss points. This relatively coarse element size limits the number of degrees of freedom (NDOF) to 61164 as well as the subsequent CPU computation time to $7.10^4 s$ for five cycles.

3.1. 3D thermal transient calculation

The details presented here correpond to TMF1 test condition. As observed experimentally, a circular heating zone of 9.5 mm radius was off-centre of 0.8 mm toward A2 loading axis in the FEA mesh, see Figure 5 and detail in Figure 5(c). This was modelled using a set of elements, to apply volumic heat source, see red area for thermal mesh, Figure 5(a). Thermal boundary conditions, Figure 5(a), take into account the convective heat flux φ_{conv} to represent air-conditioning in the testing room and the radiation heat flux φ_{rad} to represent radiation losses at high temperature: $\varphi_{rad} = \sigma\varepsilon(T^4 - T_{ext}^4)$ assuming an emissivity $\varepsilon = 0.6$ constant with temperature. To represent clamping jaws water cooling, temperature T_{jaw} is prescribed to 35 °C. Finally, induction heating is controlled with a volumetric heat flux φ_{heat} associated to a temperature regulation on a node located at the location of the LASER pyrometer, see black marker in Figure 5(a) and (c). Thermal transient calculation was analyzed for five thermal cycles.

3.2. 3D mechanical elasto-viscoplastic calculation

The mechanical behaviour is described through a "two potentials" Chaboche model [47], see Table 6, in order to describe strain rate impact on the mechanical state: two Norton flow functions are used corresponding to high and low strain rate (quick and slow terms respectively) [48]. The total strain, $\underset{\sim}{\varepsilon}^{tot}$, being the sum of mechanical strain, $\underset{\sim}{\varepsilon}^{m}$ and thermal strain, $\underset{\sim}{\varepsilon}^{th}$, these terms being function of the local temperature assessed by thermal transient analysis. The mechanical strain is also decomposed into an elastic term, $\underset{\sim}{\varepsilon}^{e}$, and a visco-plastic one, $\underset{\sim}{\varepsilon}^{p}$.

Thermomechanical FEA was modeled into three steps. The first one corresponds to the experimental thermal calibration including heating, holding time at high temperature and cooling steps with zero force at boundaries A1, A2, B1 and B2. The second step models the heating with again zero force at A1, A2,

Table 6: Governing equations of the "Two potentials" behavior used for Ha188.

Strain partitioning	$\underset{\sim}{\varepsilon}^{tot} = \underset{\sim}{\varepsilon}^{e} + \underset{\sim}{\varepsilon}^{p} + \underset{\sim}{\varepsilon}^{th}$
Yield function	$f = \sqrt{\frac{3}{2}(\underset{\sim}{s} - \underset{\sim}{X}) : (\underset{\sim}{s} - \underset{\sim}{X})} - \sigma_y - R$
Kinematic hardening	$\dot{\underset{\sim}{\alpha}} = \dot{\underset{\sim}{\varepsilon}}^{p} - \gamma \underset{\sim}{\alpha} \dot{p}$ $\dot{\underset{\sim}{X}} = \frac{2}{3} C \dot{\underset{\sim}{\alpha}}$
Isotropic hardening	$R = R_0$
Flow function	"quick" term $\dot{p}_q = \langle \frac{f}{K_N^q} \rangle^{N^q}$ "slow" term $\dot{p}_s = \langle \frac{f}{K_N^s} \rangle^{N^s}$
Total cumulated plasticity	$\dot{p} = \dot{p}_q + \dot{p}_s$

B1 and B2, while the maximum temperature is reached for the first time. At this point, displacements at boundaries A1, A2, B1 and B2 were set to zero, in the direction normal to each boundary consistently with experiment. In a third step, five anisothermal cycles have been considered with the boundary conditions described Figure 5(b), keeping zero displacement on A1, A2, B1 and B2.

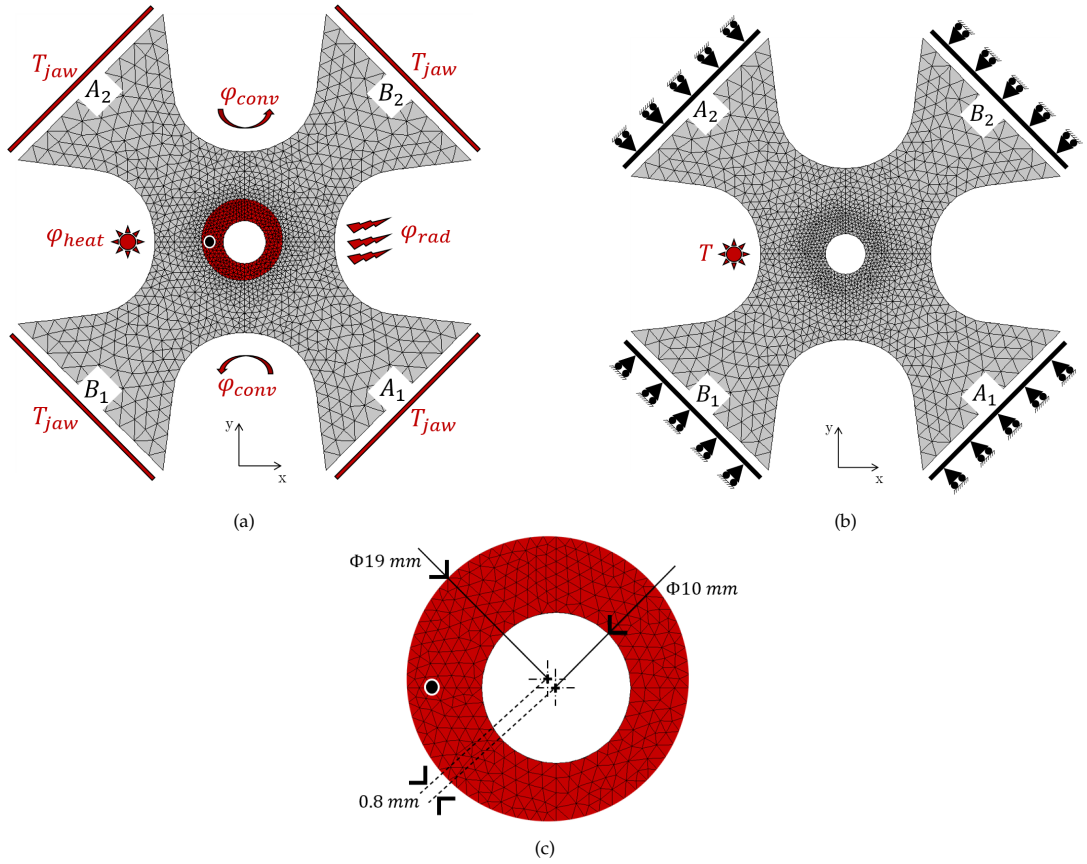

Figure 5: Meshes and boundary conditions used to model TMF1: (a) 3D thermal transient FEA; (b) 3D mechanical FEA; (c) Detail around the central hole showing the off-centre set of elements used for volumetric heat flux, black circle in (a) and (c) corresponds to the location of the node used for temperature regulation so as to mimic pyrometer.

4. Experimental and numerical analysis of thermomechanical behaviour

To clarify both experiment and quality of model, TMF1 condition will be detailed in the sequel.

4.1. Temperature cycling and temperature field

Temperatures evolution corresponding to thermocouples (TCs) and pyrometer measurements were plotted Figure 6(a) as a function of time. For the sake of clarity, only temperature evolution corresponding to pyrometer, TC1, TC2, TC7 and TC8 are plotted and their locations are displayed on the IRT cartography, Figure 6(b) and (e) and Table 3. First, it is clear that the temperature control through pyrometer was efficient considering minimum, maximum and linearity of temperature evolution. Secondly, for colder areas, a noticeable offset is observed together with non-linear temperature evolution, associated to thermal

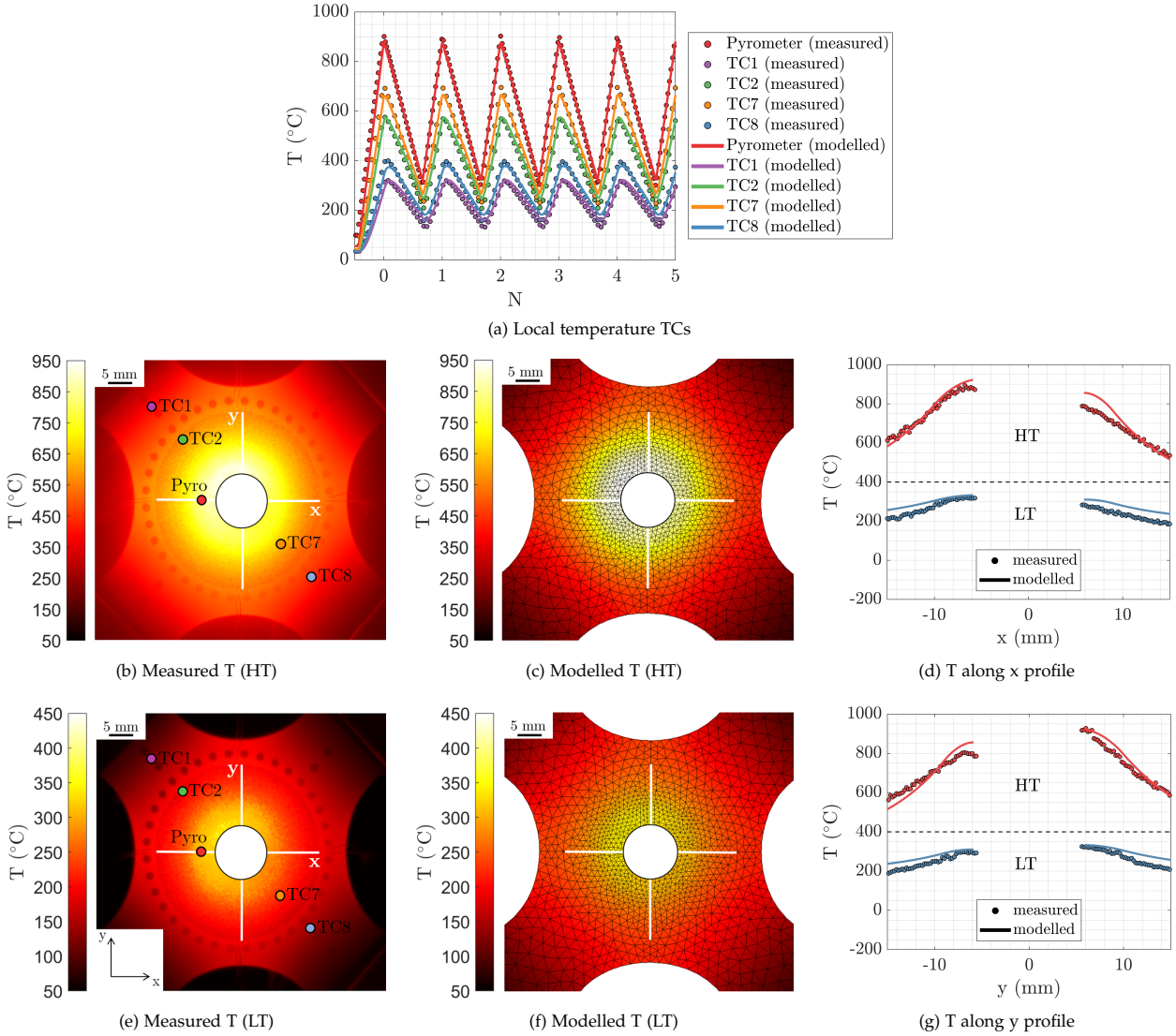

(a) Local temperature TCs

(b) Measured T (HT)

(c) Modelled T (HT)

(d) T along x profile

(e) Measured T (LT)

(f) Modelled T (LT)

(g) T along y profile

Figure 6: Temperature analysis of TMF1 from experiment and FEA: (a) Evolution of temperature (T) with time for thermocouples and pyrometer for the first five cycles; Temperature fields at maximum heating condition ($T_{pyro} = 900\,°C$), defining high temperature (HT): (b) Measured by IRT and (c) Modelled by FEA; and temperature fields at minimum heating condition ($T_{pyro} = 300\,°C$), defining low temperature (LT): (e) Measured by IRT and (f) Modelled by FEA; Measured and modelled temperature evolutions at HT and LT: (d) Along axis x (g) Along axis y.

diffusion. Despite this non-linear behavior, it is obvious that the cycles after first heating are very similar to each other. Regarding temperatures evolution on thermocouples, Figure 6(a), whether it is a hot area (TC7-orange) or a cold area (TC1-purple), both are well modelled.

Local temperature fields measured by IRT and modelled by FEA for the second thermomechanical cycle are represented respectively Figures 6(b) and (e) and Figures 6(c) and (f). Figures 6(b) and (c) show the experimental and FEA temperature fields at maximum heating conditions, whereas Figures 6(e) and (f) show the experimental and FEA temperature fields at minimum heating conditions respectively. It is worth noting that experimental temperature fields, Figures 6(b) and (e), highlight a heating off-center toward the upper left corner of the central hole. The comparison of temperature fields measured by IRT and modelled by FEA highlights the consistency for both high and low temperature results as well as the off-center heating thanks to the modelling strategy detailed above, see section 3.1.

This last observation is further validated by experimental and simulated temperature plot along profiles x and y for both minimum and maximum heating conditions, Figures 6(d) and (g), where a significant difference of temperature is observed close to the central hole at maximum and minimum heating conditions from side to side of the hole (compare -5 and 5 mm locations on axes x and y). The same figures emphasise the temperature gradient during the TMF test, the measured gradients being of $30\,^{\circ}\mathrm{C\,mm^{-1}}$ and $10\,^{\circ}\mathrm{C\,mm^{-1}}$ respectively at maximum and minimum heating conditions. The agreement in measured and modelled temperature gradient is very good regarding the complexity of the temperature condition, the root mean square error being of 35 °C and 21 °C respectively at maximum and minimum heating conditions.

4.2. Mechanical cycling and strain field results

The evolution of force as a function of relative elongation is first analyzed in a given direction. The relative elongation is based on the virtual extensometer defined by markers, see black square boxes Figure 7(c) and (f), in the direction corresponding to θ=135°, direction A1-A2 in Figures 1(b) and 5(b). Force evolution is plot as a function of this relative elongation, $\frac{\Delta L}{L_0}$, Figure 7(a). From this plot, hysteresis on cycling could be associated to generalised plasticity. This hysteresis is reached as soon as displacements are prescribed to zero, see first cycle in green, and this plasticity is sustained on cycling, see second cycle in blue.

In addition to that, the evolution of local ortho-radial mechanical strain, $\varepsilon^m_{\theta\theta}$, function of pyrometer temperature has been plotted Figure 7(b). The first heating, see red points, yields to compressive straining due to temperature gradient. The OP-TMF loading is emphasised when displacements are set to zero, see green and blue points, where strain is maximal at minimum heating conditions and minimal at maximum heating conditions. At this macroscopic level, the consistency between model and experiment are satisfactory for temperature, global relative elongation and local ortho-radial mechanical strain amplitude, Figures 7(a) and (b).

The field of displacement through the whole specimen during anisothermal test is obtained thanks to DIC results. The subset of images were sized to 31 pixels and a step was sized to 7 pixels to track the displacement between images, yielding a resolution of 180 µm.

The local mechanical strain ε^m is deduced from the difference between total strain, ε^{tot}, measured by DIC and thermal strain, ε^{th}, derived from local temperature measured by IRT, namely $\varepsilon^m = \varepsilon^{tot} - \varepsilon^{th}$ with $\varepsilon^{th} = \alpha(T)(T - T_{ref})$ with α the coefficient of thermal expansion and T_{ref} corresponding to room temperature. Because the resolution of the IRT is lower than the DIC ones, the temperatures measured by the IRT were interpolated to the DIC measurement points in order to calculate the mechanical strain field, ε^m.

Figures 7(c) and (d) show the experimental and FEA ortho-radial mechanical strain fields at maximum heating conditions, whereas Figures 7(f) and (g) show the experimental and FEA ortho-radial mechanical strain fields at minimum heating conditions respectively. Local mechanical strain at maximum heating conditions, Figure 7(c), pointed out maximum absolute mechanical strain ($\varepsilon^m_{\theta\theta} = -0.9$ %) where the heating is off-center (for $90 < \theta < 180°$). Local mechanical strain at minimum heating conditions, Figure 7(f) exhibits four major locations of strain localisation at the edge of the central hole toward specimen fillets

(lines u and v). Finally, the agreement of the model with the experiment in terms of strain localisation is excellent at the edge of the hole at high temperature, but with a slight deviation of the angular location of maximum local strain at low temperature (compare Figure 7(c) to (d) and Figure 7(f) to (g) respectively).

To detail this comparison, strain profiles are analysed at the location of the angles associated to the measured and modelled maximum local mechanical strain, namely along lines u and v, Figures 7(e) and (h). Absolute mechanical strain level is observed to be higher at maximum heating conditions where the maximum level of compression is reached. Despite this high compression level, no buckling of the thin-sheet specimen was observed. Figures 7(e) and (h) highlight the severe thermomechanical gradient of the TMF test with the variation of mechanical strain amplitude along profiles u and v, at both low

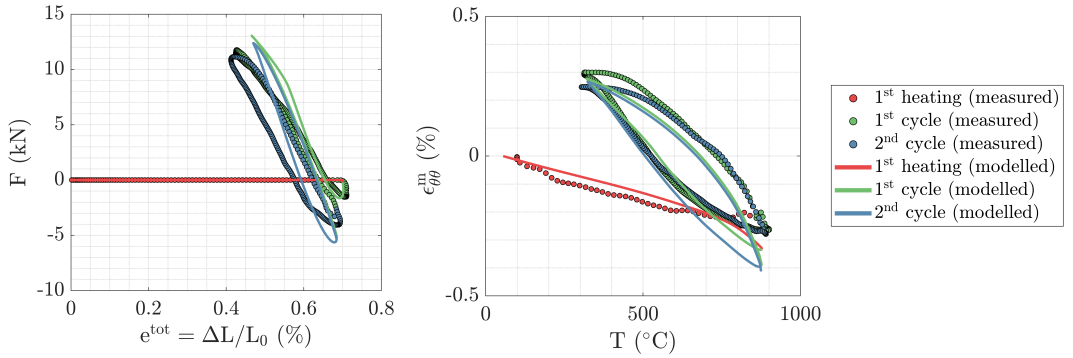

(a) Force function of global strain $\frac{\Delta L}{L_0}$

(b) Local strain $\varepsilon^m_{\theta\theta}$ function of T

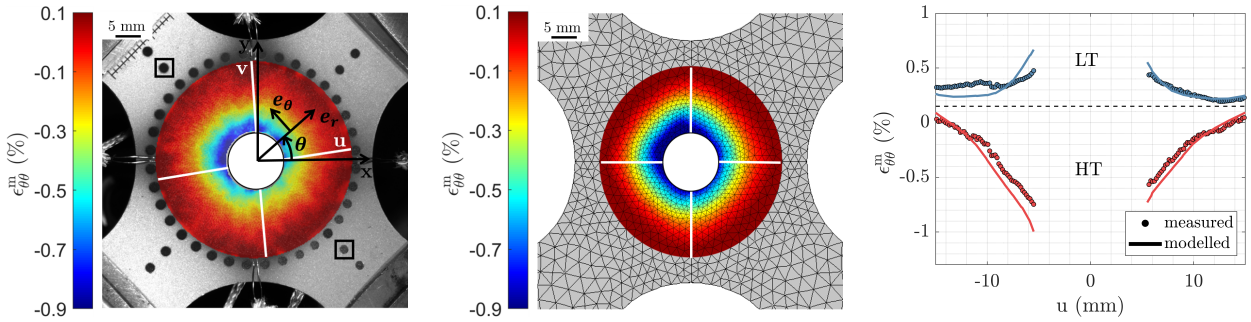

(c) Measured $\varepsilon^m_{\theta\theta}$ (HT)

(d) Modelled $\varepsilon^m_{\theta\theta}$ (HT)

(e) $\varepsilon^m_{\theta\theta}$ along u profile

(f) Measured $\varepsilon^m_{\theta\theta}$ (LT)

(g) Modelled $\varepsilon^m_{\theta\theta}$ (LT)

(h) $\varepsilon^m_{\theta\theta}$ along v profile

Figure 7: Mechanical strain field analysis of TMF1: Measured and modelled thermomechanical loading hysteresis curves for first heating (without mechanical constraint) and TMF cycles 1 & 2: (a) Force function of relative elongation; (b) $\varepsilon^m_{\theta\theta}$ function of pyrometer temperature; Ortho-radial mechanical strain $\varepsilon^m_{\theta\theta}$ fields at HT: (c) Measured by DIC; (d) Modelled by FEA; and $\varepsilon^m_{\theta\theta}$ LT: (f) Measured by DIC; (g) Modelled by FEA; Measured and modelled ortho-radial mechanical strain evolution at HT and LT: (e) Along axis u and (h) Along axis v.

temperature (see LT blue curve) and high temperature (see HT red curve). Despite local errors in strain level, the strain gradients are consistent between FEA and experiment, Figures 7(e) and (h).

5. Experimental analysis of damage localisation and micro-crack growth rate

5.1. Experimental micro-cracks field characterisation by machine learning

The ML model trained on one SEM image as detailed above, see section 2.6, was applied to assess final damage field of TMF1 specimen after 200 cycles. This image segmentation was performed on a 4000x4000 pixels image representing the entire hole of the specimen reconstituted by stitching of 35 SEM images yielding a resolution of 4 µm, see Figure 8(a). This provides the measurement of 403 micro-cracks initiated on the front face of the specimen during the test. These cracks are located all around the central hole, their observations are improved by the fact that room temperature, tensile stresses open these cracks. The measured micro-cracks density was interpolated between elements of the mesh detailed in section 3, see Figure 5, following a natural neighbor interpolation to obtain a damage field, see Figure 8(b). From this measurement of damage field, it can be concluded that the damage is highly localized at one hotspot of the edge of the hole, corresponding to a major crack of 740 µm long observed in the rectangular box Figure 8(a). More limited damage, corresponding to smaller micro-cracks, are distributed all along the central hole. The damage localization pattern appears to be correlated to both maximum strain measurement at maximum temperature and the strain localization at minimum temperature, compare 8(b) to Figure 7.

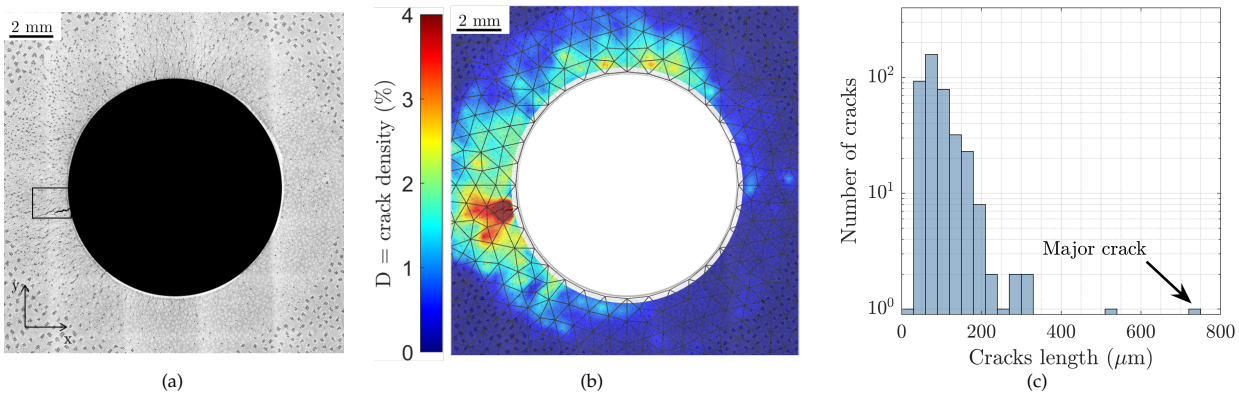

(a) (b) (c)

Figure 8: Micro-crack post-mortem analysis of TMF1: (a) Stitched SEM images before analysis; (b) Result of ML algorithm, displayed as micro-cracks density field based on the FEA mesh; (c) Histogram of micro-cracks according to their length.

Micro-cracks detected by ML are converted into ellipses using ImageJ, the major axis of ellipsis being assumed to provide a good assessment of the length of each micro-crack [49]. Considering relatively straight path of these micro-cracks, Figure 4, this assumption seems sounded. As a result of ML, Figure 8(c) shows a histogram of the number of micro-cracks according to their length. The crack detection yields to an average crack length of 92 µm for a standard deviation of 58 µm.

5.2. Micro-crack growth measurement by digital image correlation

A local displacement field acquisition at the crack scale length was analyzed, using the third camera located in the central axis of the specimen, aligned with the central hole Figure 3. As detailed in section 2.2 and Figure 1(b), a cylindrical coordinates system is based on the center corresponding to the center of the specimen. From this axes system, ortho-radial displacement U_θ can be measured, here at minimum heating condition.

Subset of images were sized to 41 pixels and a step was sized to 8 pixels yielding to a resolution of 60 µm, see Appendix A for sensitivity analysis. On this basis, micro-crack growth could be assessed by the detection of maximum local gradient of ortho-radial displacement U_θ, [18, 19]. Micro-crack growth measurement is described here for the TMF1 test.

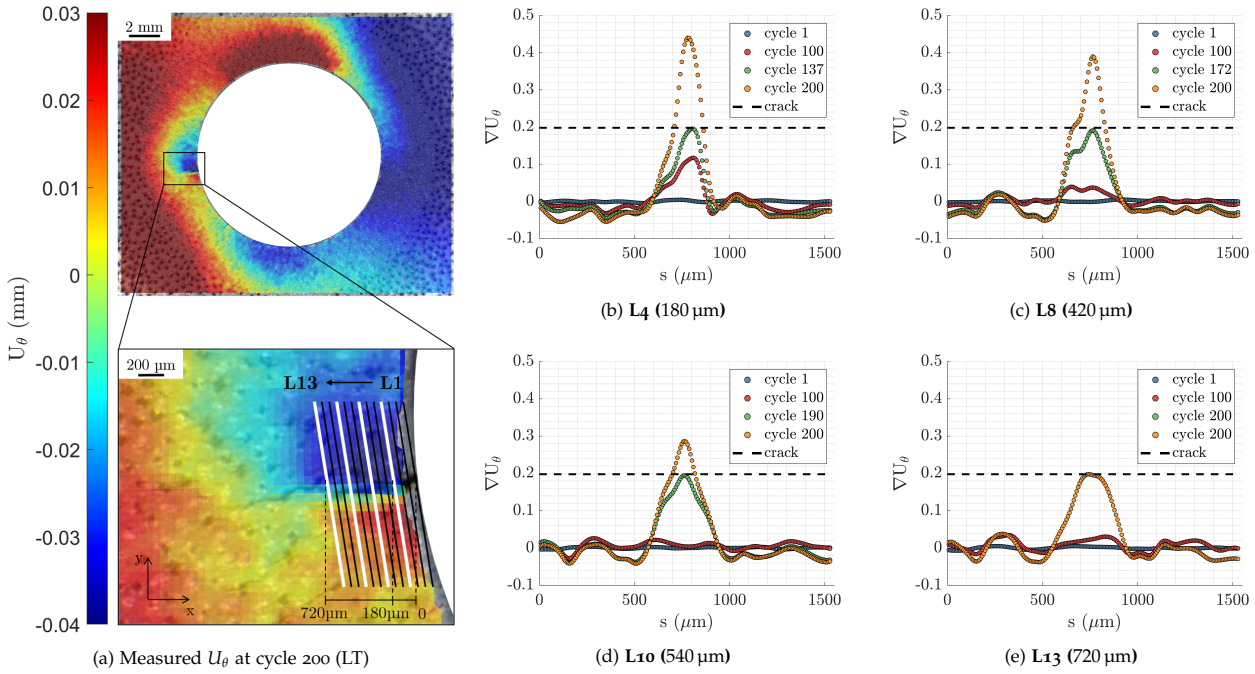

(a) Measured U_θ at cycle 200 (LT)

(b) **L4** (180 µm)

(c) **L8** (420 µm)

(d) **L10** (540 µm)

(e) **L13** (720 µm)

Figure 9: Displacement analysis for crack detection of TMF1: (a) Displacement field U_θ in the vicinity of the hole at the 200^{th} cycle and low temperature, rectangle highlights the location of the analysis, detailed in zoom with lines L1 to L13 ; ∇U_θ measured for several cycles at (b) Line L4 (180 µm); (c) Line L8 (420 µm); (d) Line L10 (540 µm); (e) Line L13 (720 µm).

To perform this detection, local gradient are analysed along lines numbered from 1 to 13, each line being of 1.5 mm long and equally spaced of 60 µm, Figure 9(a) and associated detailed views. Local gradient is defined as:

$$\nabla U_\theta \simeq \frac{\Delta U_\theta}{\Delta s} \tag{5}$$

Δs being the distance between two successive analysed points on the lines L1 to L13.

A criterion for gradient associated to a crack crossing one line should be determined. From lines L1 to line L3, the noise to signal ratio induced by edge effect is too high to achieve robust displacement measurement by DIC. The first line to be considered is the line L4, located at 180 µm from the edge of the hole, Figure 9(b). For this line L4, local oscillations at cycle 1 should be associated to noise level, see blue markers in Figure 9(b). On the other hand, at cycle 200 the chosen gradient evidences the presence of the crack where physical jump in displacement appears as a maximum of local gradient of displacement, see orange markers in Figure 9(b). Based on the final crack length measured ex situ by ML, a crack initiation threshold for detection for $\nabla U_\theta = 0.2$ has been set to reach a final crack consistent in length between DIC and ML based on the gradient at line L13 corresponding to 720 µm. With this method, fatigue crack growth and fatigue crack growth rate (FCGR) can be assessed, see red markers for this TMF1 test in Figures 10(a) and (b) respectively detailed in the following section 6.1.

6. Validation and lifetime modelling methodology

6.1. Validation of the experimental method for thermomechanical fatigue loading

To validate the method developed in this paper, the full-field analysis was also applied to the TMF2 test condition described in section 2.2 and in Table 4. By varying the temperature control point location with the pyrometer, the local variation of temperature ΔT, as well as the temperature at maximum and

minimum heating conditions of the OP-TMF cycle were modified: temperature was ranging from minimal to maximum heating condition, from 330 to 890 °C for TMF1 and from 300 to 860 °C for TMF2 at the location of the main crack analysed respectively for each test.

Local strains measured at the same location correspond to $\max(\varepsilon^m_{\theta\theta}) = 0.5 \pm 0.05\%$, $\min(\varepsilon^m_{\theta\theta}) = -0.9 \pm 0.05\%$ and $\Delta\varepsilon^m_{\theta\theta}/2 = 0.7 \pm 0.05\%$ for both TMF1 and TMF2.

With the proposed micro-crack growth measurement method by DIC, section 5.2, fatigue crack growth and fatigue crack growth rate (FCGR) can be assessed. This has been carried out for TMF1 and TMF2, see red and green markers respectively in Figures 10(a) and (b). Considering, first robust detection of crack, associated to a crack length of 180 µm line L4 in Figure 9(b), the associated number of cycles is similar for both TMF1 and TMF2, Figure 10(a). For longer crack, a slight deviation occurs between the two conditions, this effect being obvious considering the FCGR: TMF1 condition yields to a slightly higher FCGR as compared to TMF2 condition, Figures 10(b).

This ranking is consistent with the maximum temperature reached during cycling, 890 °C and 860 °C for TMF1 and TMF2 respectively. Even though, this difference in temperature is not that high, the drop in mechanical properties of Ha188 beyond 800 °C is noteworthy, see Table 2.

This could be seen as a first validation of the set-up and measurement methodology, especially the crack length measurement based on gradient of displacement: on the one hand, close experimental conditions induce similar damage behaviour, on the other hand, the high resolution of the method enables to distinguish variations induced by local temperature.

6.2. Comparison of thermomechanical fatigue results to isothermal fatigue results

Before considering micro-crack growth model, we propose here to compare the database obtained in isothermal condition to the results obtained in TMF conditions as described above. The isothermal test series corresponds to a broad range of applied strain levels at 900 °C. To further compare OP-TMF testings to isothermal test series, it is straightforward to measure strain level using a virtual extensometer within a gage length of 10 mm consistent in size with the gage length used for isothermal testing. This results in $\Delta\varepsilon^m/2 = 0.4\%$ for both TMF1 and TMF2 tests. At this macroscopic level, TMF testing amplitudes correspond to $0.375\% < \Delta\varepsilon^m/2 < 0.75\%$, Table 4 detailed in section 2.2.

Grey points in Figure 10(a) correspond to isothermal test series. This shows the micro-cracks growth function of the number of cycles, exhibiting a large range in terms of number of cycles to reach a long crack regime. The effect of strain ratio is rather limited for the tested material, the observed lifetime being clearly a function of $\Delta\varepsilon^m/2$, see Table 7. For LCF test series, the lifetime is chosen here to be the number of cycles required to reach a crack length of 420 µm measured by optical means. This value corresponds to

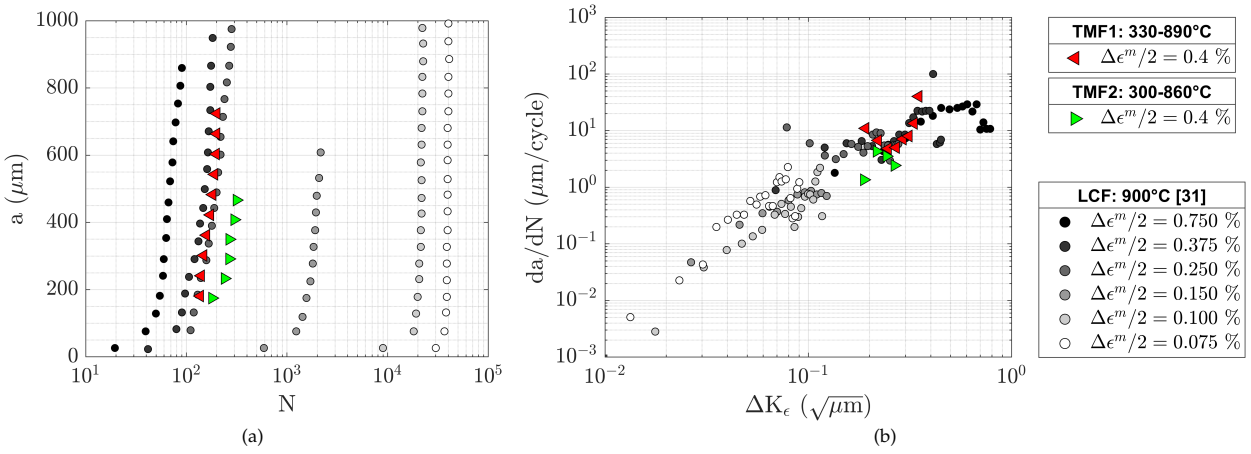

Figure 10: Micro-crack growth for TMF1, TMF2 and LCF [31] loadings: (a) Micro-crack length function of the number of cycles N; (b) Micro-crack growth rate da/dN function of ΔK_ϵ.

Table 7: $\Delta\varepsilon^m/2$ and number of cycles to reach a cracl length of 420 µm for OP-TMF testing from this study and for isothermal LCF testing from [31]; for OP-TMF the temperature corresponds to the measured temperature at major crack location.

Name	T (°C)	$\Delta\varepsilon^m/2$ (%)	N_f	Reference
TMF1	330-890	0.4	172	This study
TMF2	300-860	0.4	302	
LCF1	900	0.075	39784	[31]
LCF2		0.100	21158	
LCF3		0.150	1956	
LCF4		0.250	190	
LCF5		0.375	147	
LCF6		0.750	64	

line L8 used for displacement gradient analysis in TMF testing, Figure 9(c), and enables to take advantage of FCGR measurement for different crack lengths. Thus, based on the gradient of displacement, the same crack length is used to consider the lifetime of OP-TMF tests TMF1 and TMF2. Lifetime of both LCF and OP-TMF tests are detailed in Table 7. Finally, the two OP-TMF tests correspond to lifetime associated to the range $\Delta\varepsilon^m/2$=0.150 − 0.20% which are lower strain values as compared to strain measured for TMF conditions.

To represent strain controlled fatigue crack growth rate, the K_ε concept is straightforward in many cases, e.g. see [50, 51], thus the Figure 10(b) shows the micro-crack growth rate function of $\Delta K_\varepsilon \simeq \Delta\varepsilon\sqrt{\pi a}$. Of course this constitutes a coarse assumption, by ignoring any correction in shape factor associated to each specimen geometry, but should be seen as an attempt to gain knowledge in FCGR sensitivity to TMF loadings. Again, for isothermal testing, consistently with the broad applied strain range, a very broad range of FCGR has been reached. Micro-crack growth rate of the tested TMF1 loading, with $\Delta\varepsilon^m/2$=0.4%, is consistent with the FCGR of 900 °C LCF tests, corresponding to the range $\Delta\varepsilon^m/2$=0.375 − 0.75%. Thus, the OP-TMF TMF1 loading seems consistent with similar condition experienced in isothermal testing. Besides, the variation of FCGR observed for TMF2 test as compared to TMF1, lies in the range of scatter observed in isothermal conditions. This again shows the consistency, on the one hand between TMF testing and isothermal test series, and on the other hand between TMF1 and TMF2.

Last but not least, we propose here to compare micro-crack patterns obtained for TMF2 condition and isothermal testing corresponding to the maximum applied strain level, namely $\Delta\varepsilon^m/2$=0.75%, Figure 11. First, a high number of micro-cracks are observed for both testing conditions. These micro-cracks being

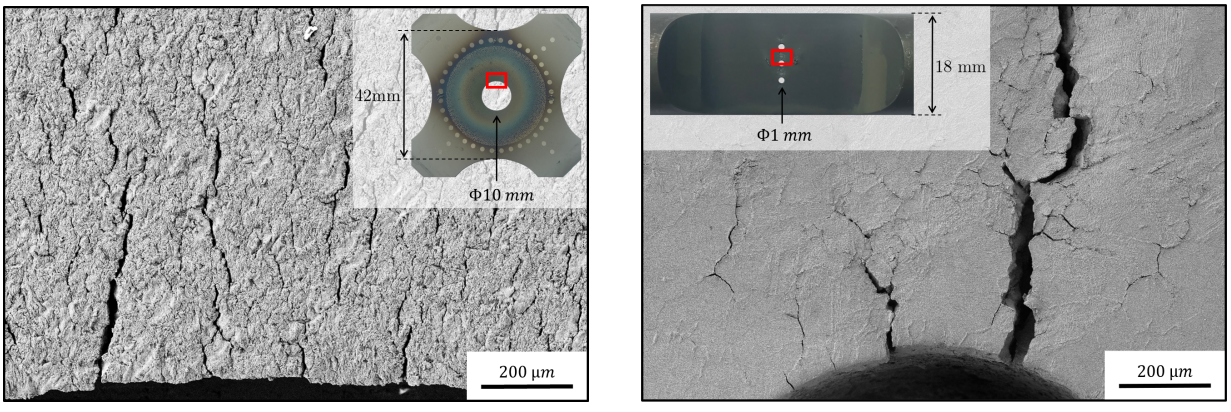

(a) (b)

Figure 11: SEM images of multi-cracking around the central hole for: (a) TMF2 ($\Delta\varepsilon^m/2 = 0.4\%$) after 315 cycles, the aspect of the alloy corresponds to sand blasting (see details in section 2.6); (b) LCF6 ($\Delta\varepsilon^m/2 = 0.75\%$) after 97 cycles, this specimen was not sandblasted.

either initiated at the edge of the hole or with an obvious distance to this hole. Secondly, it is worthy that the shape of most of micro-cracks could be associated to intergranular damage mechanisms.

These similarities, between TMF and isothermal conditions in both micro-crack mechanisms and range of FCGR, help to gain confidence in further comparison in terms of fatigue crack growth rate and lifetime models.

6.3. Lifetime assessment by micro-crack growth model based on the partition of strain energy

Because thermal strain gradients drive the mechanical state, and that strain amplitudes are associated to LCF domain, stress based damage models are not relevant. Besides, the consistency between OP-TMF test and isothermal test series in terms of FCGR, indicates that similar driving forces can be considered. It is worth noting that the K_ε criterion shows some limitations, especially here for low strain level: for $\Delta\varepsilon^m/2 = 0.075\%$, the FCGR is higher than for $\Delta\varepsilon^m/2 = 0.1\%$, Figure 10(b). Thus, a distinction should be made between small and large scale yielding conditions to gain in consistency as a function of the applied strain level. A lifetime analysis for this LCF test series was previously performed using a micro-crack growth model based on the partition of strain energy into a hydrostatic part of the elastic strain energy, W_e, and the deviatoric part of the plastic strain energy, W_p [52, 31, 29], namely:

$$W_e = \frac{1}{3}\int_{cycle} \langle tr(\underset{\sim}{\sigma})\rangle . \langle tr(d\underset{\sim}{\varepsilon}^e)\rangle \tag{6}$$

$$W_p = \int_{cycle} \underset{\sim}{s} : d\underset{\sim}{\varepsilon}^p \tag{7}$$

where $\underset{\sim}{\sigma}$, $\underset{\sim}{\varepsilon}^e$, $\underset{\sim}{s}$ and $\underset{\sim}{\varepsilon}^p$ are respectively the stress tensor, the elastic part of the strain tensor, the deviatoric part of the stress tensor and the inelastic part of the strain tensor. The Mackaulay brackets $< f >$ correspond to the positive part of the tested function f, that is to say that $< f >= f$ if $f > 0$ and $< f >= 0$ otherwise.

On this basis, the contribution of two power law functions yields the FCGR model:

$$\frac{1}{\lambda}\frac{da}{dN} = \left(\frac{w_e^*}{\gamma_e}a\right)^{m_e} + \left(\frac{w_p^*}{\gamma_p}a\right)^{m_p} \tag{8}$$

where λ, γ_e, γ_p, m_e and m_p are model parameters function of the considered material.

Terms w_e^* and w_p^* correspond to a simple non local analysis which consists in averaging energy terms in a chosen volume to get rid of mesh size dependency [29]. In this study, quadratic element sized to 1 mm including four Gauss points are used in the region of interest for the sake of computation cost. Therefore, the area of influence of one Gauss point is nearly 300 µm, this value could be compared to an averaging achieved on a sphere of a radius of 300 µm for which fatigue crack growth model parameters have been previously identified.

The crack growth rate equation 8 is integrated using a Runge-Kutta type algorithm, the lifetime N_f being assessed by micro-crack propagation from initial to final crack length, a_0 to a_f, according to:

$$N_f = \int_{a_0}^{a_f} \frac{da}{\left(\frac{da}{dN}\right)} \tag{9}$$

We set a_0 and a_f considering an initial micro defect a_0 sized to 1 µm, corresponding to the value of a_0 set for LCF tests lifetime prediction in [31], and a final crack length a_f sized to 420 µm, corresponding to the lifetime defined for TMF and LCF tests in section 6.2. Parameters used in this study for the micro-crack growth model based on the partition of strain energy are summarised in Table 8.

Table 8: Parameters used for the micro-crack growth model based on the partition of strain energy [31, 29].

$\lambda\ (m)$	$\gamma_e\ (J.m^{-2})$	m_e	$\gamma_p\ (J.m^{-2})$	m_p	$a_0\ (m)$	$a_f\ (m)$
$90\ 10^{-6}$	11500	1.5	280000	0.9	$1\ 10^{-6}$	$420\ 10^{-6}$

The experimental damage field D was derived from the micro-cracks density measured by ML, Figure 12(a) and (d) for TMF1 and TMF2 tests respectively. These damage fields are very similar considering the offset for angles $\theta \simeq 135°$, but differ in the area of high damage level, which is higher for TMF1 than for TMF2. This result is consistent with the higher FCCR observed for TMF1 than for TMF2, Figure 10(b).

The TMF2 model is the same as detailed above for TMF1 (thermal FEA and then mechanical FEA), the only difference being the location of the point used to model pyrometer location, and control loop for temperature as a function of time, consistently with experiment.

For both TMF1 and TMF2, the modelled damage field is associated to the number of cycles to failure N_f obtained by the energy model by $D = 1/N_f$, Figure 12(b) and (e) for TMF1 and TMF2 conditions respectively. Model damage field is consistent in maximum location, but is clearly over-assessed at some points.

To get more details about damage, Figure 12(c) shows the magnitude and localisation of damage D/D_{max} along a circular profile of 6 mm in radius for both TMF1 test and related FEA. The modelled damage localisation is observed to be consistent with the experimental one, especially for angles about 80-90° and 180-190° with a typical offset in damage localisation about 5°. The model overestimates damage level for points located at angles around 0 and 270°, Figure 12(c). Moreover, the crack initiation detection method based on discontinuous displacements from DIC measurement exhibits a 420 µm micro-crack length after 172 cycles, whereas for the same crack size, the lifetime energy based model predicts a

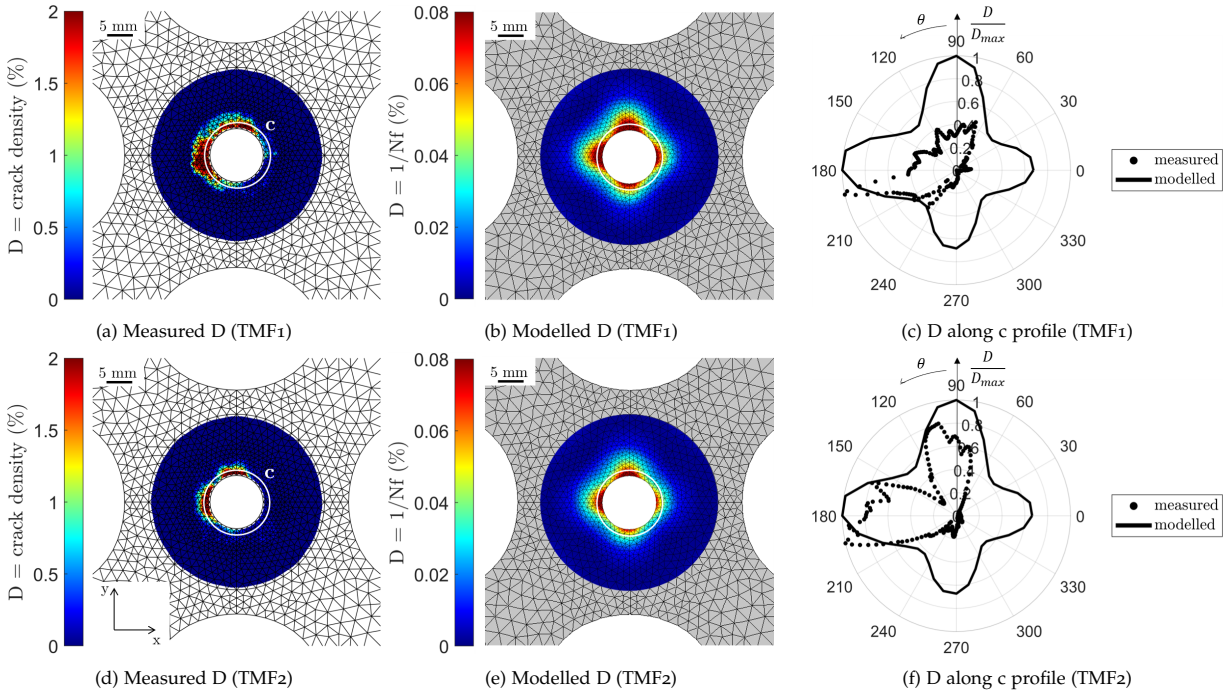

(a) Measured D (TMF1) (b) Modelled D (TMF1) (c) D along c profile (TMF1)

(d) Measured D (TMF2) (e) Modelled D (TMF2) (f) D along c profile (TMF2)

Figure 12: Damage analysis for TMF1: (a) Micro-cracks density field obtained by ML post-test; (b) Modelled $D = 1/N_f$ obtained by the energy model; (c) Measured and modelled damage D/D_{max} along a circular path of 6 mm radius; Damage analysis for TMF2: (d) micro-cracks density field obtained by ML post-test; (e) Modelled $D = 1/N_f$ obtained by the energy model; (f) Measured and modelled damage D/D_{max} along a circular path of 6 mm radius.

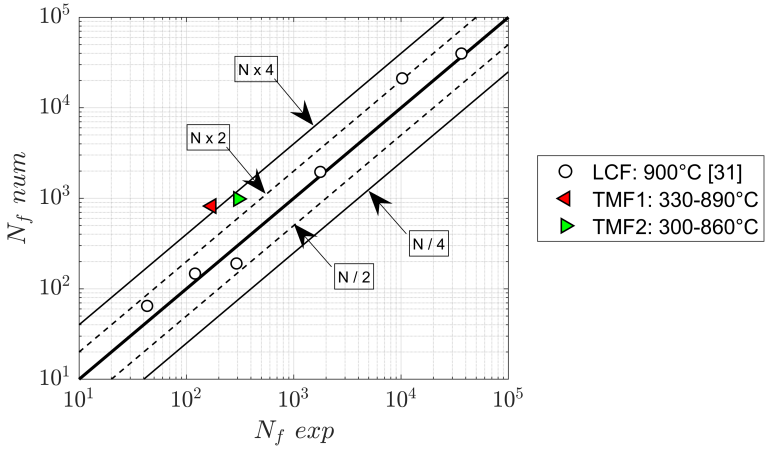

Figure 13: Comparison between the modelled (N_f *num*) and the experimental (N_f *exp*) number of cycles to reach a_f for TMF1, TMF2 and LCF [31] loadings; dashed lines and thin lines correspond respectively to a factor of two and four compared to experimental observation [31, 29].

lifetime of 821 cycles. This overstimation in lifetime appears to be consistent with the observed detrimental effect of TMF condition as compared to isothermal ones. Besides, the angular offset in damage is similar to the one observed for strain localisation, compare Figure 12(a) to Figure 7(f).

For TMF2 test condition, the damage field is similar to the one observed experimentally, Figure 7(f), with a closer assessment of damage level at maximum damage locations (around angles of 90° and 180°) as compared to TMF1.

Finally, comparison of OP-TMF conditions to isothermal testing is plot in a log-log plot of lifetime assessment as a function of experimental lifetime, Figure 13. The isothermal LCF results are lying in the band $N_f/2$ to $N_f \times 2$, see black empty circles, whereas the TMF results are lying in the band $N_f/4$ to $N_f \times 4$, see colored triangles. Although the model successfully provides a suitable order of magnitude of lifetime, it tends to overestimate the observed TMF results. On the one hand, this confirms the ability of the proposed model to assess lifetime from strain energy partitioning, even for OP-TMF loading in a first attempt. On the other hand, the over-assessment of lifetime is fully consistent with detrimental effect of this TMF loading as compared to isothermal one.

7. Discussion

This discussion will first be focused on the benefit of the chosen methodology in terms of resolution of full-field approaches for very high temperature, and then on the contribution of this method to assess the quality of the finite element analysis. Finally, new data for the Ha188 material in terms of lifetime and fatigue crack growth in OP-TMF conditions will be discussed.

The above set-up yields some high resolution DIC thanks to LASER engraving adapted to both very high temperature and to the targeted spatial resolution. The LASER engraving was previously successfully tested only at 500 °C in [53], and is validated in the present study for the first time up to 900 °C. The macroscopic resolution of displacement is of about 180 µm. Local DIC resolution is of about 60 µm. On this basis, the analysis of gradient of displacement induced by micro-cracking has been achieved yielding a crack resolution of about 60 µm in length. In the reference work of Wang et al. [54], authors have obtained similar resolution for crack size detection (of about 70 µm), but for much lower temperature of test in the range [400-600]°C. Thus, the set of experimental data obtained in the present study yields for the first time the possibility to describe both fatigue crack growth and local strain driving this crack in a thin sheet from low to above 900 °C using in situ measurement. This constitutes a major step for high temperature testing for which most of experiments are using large markers and flags measurement for macroscopic strain analysis [55].

To validate the in situ crack measurement, ex situ micro-cracks quantification by machine learning (ML) yields robust crack analysis considering the large number of micro-cracks detected, and the accuracy in the crack length detection. It is worth noting that the training set for ML could be achieved on a single image, and is robust enough of course for the set of 35 images toggled together in the present study to obtain the full-field of view, but also to other tests executed on the same material with SEM images to be analysed. From SEM analysis and ML, the associated spatial resolution for crack detection is of about 4 µm in length, and the difference in crack length between in and ex situ is of about 20 µm. This method based on gradient of displacement could face some artefact by the high micro-crack density observed experimentally: the gradient measurement could indeed be the result of several micro-cracks crossing the line chosen for displacement analysis. This pushes also the need to include ML in DIC tools so as to improve the detection of crack.

On the other hand, quality of FEA was improved by controlling both temperature field (by adjusting heat source and exchange values), and temperature evolution with time (by closed-loop controlling the pyrometer point to mimic experiment). Without further fitting of the mechanical behavior model, an excellent consistency was obtained between experiment and numerical analysis both for macroscopic values (force and displacement at markers) and local values (strain fields). However, some observed differences in the angular location, as well as differences in level of maximum strain, should be associated to either local variations of temperature field, emissivity variation and subsequent local variation of strain. Because after calculating damage by ML, the location of the angular deviation related to the maximum damage is similar to the one related to maximum strain, this could be the consequence of a modification of thermal field during experiment. However, gradients are carefully described by FEA, demonstrating the quality of both measurement and model regarding the complexity of the environment. Thus, simultaneous measurement of temperature by IRT and local displacement by DIC will help in improving these aspects. As compared to the state-of-the-art where most of authors have tried to decrease temperature gradient in biaxial TMF facilities [32, 56], the present study takes advantage of these gradients.

Last but not least, for the OP-TMF tested conditions, the associated FCGR of Ha188 material is very close to FCGR measured for isothermal strain-controlled testing at the maximum temperature of the OP-TMF test. Whereas, for most of Ni-based superalloy, FCGR of long crack for TMF condition lies between the FCGR associated to the minimum and maximum temperatures of the considered TMF cycle [57, 58]. For the studied Ha188 material, existing literature data are scarce for OP-TMF loading. Bonacuse and Kalluri [59], have tested isothermal fatigue, and IP and OP-TMF conditions for maximum temperature of 760 °C and minimum temperature of 316 °C. The chosen methodology uses tubular specimens, and as a failure criterion a load drop of 10 %. For these conditions, both IP and OP-TMF testings yield to similar lifetime as compared to pure cyclic testing for $\Delta\varepsilon^m/2$=0.4 % at the maximum temperature of the TMF test. In the same way, the present study shows that damage should be associated to a large extent to the maximum temperature of the TMF cycle exhibiting a detrimental effect of OP-TMF compared to LCF isothermal testing. This is quite surprising considering the fact that, at the maximum temperature of 900 °C, clear modification of damage mechanisms is observed where oxidation and creep damage should impact the intergranular cracking. Thus the OP-TMF condition should be driven by cumulated damage and plasticity in high temperature condition, and cracking within low temperature part of the cycle where tension occurs. However, because both damage mechanism and FCGR are very similar in OP-TMF and maximum temperature testing, considering a microcrack growth model identified at the maximum temperature of the TMF cycle is sounded. The observed differences in lifetimes between the experimental and numerical results for the TMF tests could be associated to an effect of thin sheet because the model identification was initially performed using bar from cast alloy. This latter promoting a 3D effect for crack initiation, that can impact the nominal crack length used to assess lifetime from FCGR [31, 29].

As a perspective of the present study, explicit meshing of crack growth could also clarify the crack closure effect, and could be straightforward to account for micro-crack network in future work [30].

8. Conclusions

An original set-up has been developed in this study, so as to perform OP-TMF testing on thin sheet material. Three major technical points are demonstrated through this work: i) the chosen testing condition enables large level of compression wihout buckling; ii) temperature gradient is designed and monitored by IRT and iii) despite oxidative environment, DIC was obtained in a robust manner using LASER engraved speckle.

This provides new tools for validating mechanical behavior and damage models, for TMF loading in gradient conditions. To measure mechanical strain fields at high temperature ($\geq 900\,^{\circ}C$), a hybrid view technique associating IRT and DIC was employed, the quality of the displacement field by DIC being improved to a large extent by a LASER engraved speckle. This enables to access to mechanical strain field with a pretty high resolution in the context of severe temperature gradient. The damage field, here associated to a density of micro-crack, was measured by ML segmentation of SEM images, images being acquired by SEM after completion of the test. The association of mechanical strain and damage at a high resolution have enabled to clarify the role of strain localisation into damage localisation. Besides, micro-crack growth was measured by coupling ex situ crack measurement by ML and in situ displacement gradients measurement by DIC. ML appears as an excellent tool to monitor damage in complex condition, the complementary with DIC improves to a large extent the resolution for crack tracking. This enables to access to FCGR and to compare the impact of OP-TMF to isothermal testing.

The thermomechanical FEA was clearly improved by the temperature control loop used to reproduce experimental temperature regulation. This yields to a straightforward assessment of thermal and mechanical conditions. On this basis, FCGR model integrated into lifetime analysis confirms the damage localisation and its correlation to strain localisation. The interest in fatigue micro-crack growth rate model has been thus demonstrated by the quality of both localisation and lifetime assessment. For the tested material Ha188, this study indicates that OP-TMF condition is close to LCF isothermal testing considering the maximum temperature of the TMF cycle. Moreover, the different OP-TMF conditions presented in this paper shows that lifetime and micro-crack growth rate is rather governed by the maximum temperature due to the substantial decrease of mechanical propreties of Ha188 over $800\,^{\circ}C$. Finally, OP-TMF on thin sheet of Ha188 is seen to be more detrimental in lifetime as compared to bulk specimen obtained from cast alloy of the same composition. This point is demonstrated by micro-crack growth analysis and integration of FCGR in the perspective of lifetime model.

In a nutshell, combining IRT, DIC with special LASER speckle and machine learning yields new possibilities in both behavior validation and identification as well as damage analysis, based on in situ measurements. Besides, the facility being able to test thin sheet in TMF and very high temperature condition, complementary tests are underway so as to clarify the impact of gradient in FCGR together with fatigue lifetime of thin sheet material testing OP-TMF and isothermal fatigue conditions.

Appendix A. Crack detection sensitivity to DIC resolution

Because DIC is involved in the crack growth detection process, the sensitivity of the method should be tested as a function of the DIC resolution. For this purpose, different subset sizes have been tested for TMF1 condition, from 31 to 71 pixels, Figure A.14. It is obvious that the largest the subset, the highest the FCGR is assessed. Besides, the minimum FCGR, well established effect of transition from small to long crack growth behavior, could only be captured for 31 and 41 pixel subset sizes. For lower subset size, the analysis is not relevant. Finally, the noise to signal ratio being improved by increasing the subset size, we chose in this study to keep 41 pixels as a reference subset size.

Acknowledgements

This paper is dedicated to the memory of Alain KÖSTER (1963-2021), Centre des Matériaux - Ecole des Mines de Paris involved in sample design, testing and also fruitful discussions on high temperature experimentation over years. We gratefully acknowledge Dimitri MARQUIÉ and Janvier LECOMTE from Safran Aircraft Engines and René CLUZET and Frédéric COUTARD of Centre des Matériaux - Ecole

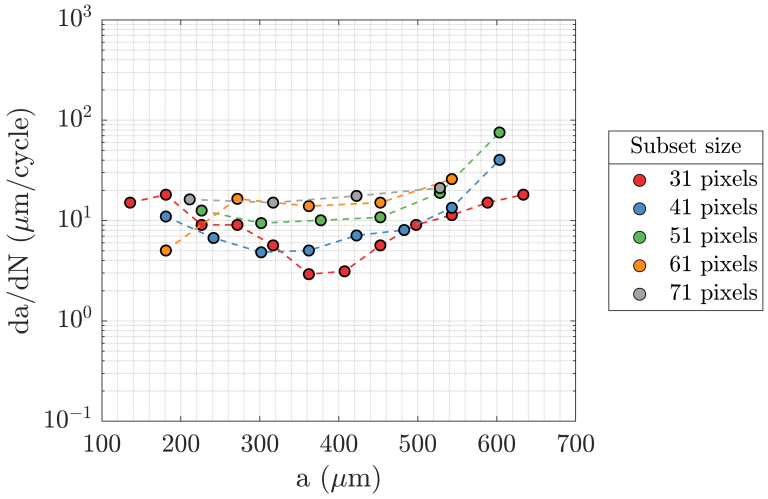

Figure A.14: Sensitivity analysis of FCGR measured by maximum local gradient technique (see section 5.2): evolution of FCGR as a function of the crack length

des Mines de Paris for sample machining. We also gratefully acknowledge Jean-christophe TEISSEDRE of Centre des Matériaux - Ecole des Mines de Paris for his experimental set-up assistance of the three synchronised cameras system with LabView script "Paul" and his python code "Ariane" for markers tracking. The authors thank Arnaud LONGUET from Safran Aircraft Engines for discussions on the "Two potentials" behavior used for Ha188 EVP calculation. This work was funded by Safran Aircraft Engines.

References

[1] L. Bodelot, L. Sabatier, E. Charkaluk, P. Dufrénoy, Experimental setup for fully coupled kinematic and thermal measurements at the microstructure scale of an aisi 316l steel, Materials Science and Engineering: A 501 (1-2) (2009) 52–60.
[2] A. Chrysochoos, V. Huon, F. Jourdan, J.-M. Muracciole, R. Peyroux, B. Wattrisse, Use of full-field digital image correlation and infrared thermography measurements for the thermomechanical analysis of material behaviour, Strain 46 (1) (2010) 117–130.
[3] A. Maynadier, M. Poncelet, K. Lavernhe-Taillard, S. Roux, One-shot measurement of thermal and kinematic fields: infrared image correlation (iric), Experimental Mechanics 52 (3) (2012) 241–255.
[4] G. Soares, N. Vázquez-Fernández, M. Hokka, Thermomechanical behavior of steels in tension studied with synchronized full-field deformation and temperature measurements, Experimental Techniques 45 (5) (2021) 627–643.
[5] Y. Wang, A. Charbal, J. Dufour, F. Hild, S. Roux, L. Vincent, Hybrid multiview correlation for measuring and monitoring thermomechanical fatigue test, Experimental Mechanics 60 (1) (2020) 13–33.
[6] J. Lyons, J. Liu, M. Sutton, High-temperature deformation measurements using digital-image correlation, Experimental mechanics 36 (1) (1996) 64–70.
[7] B. Grant, H. Stone, P. Withers, M. Preuss, High-temperature strain field measurement using digital image correlation, The Journal of Strain Analysis for Engineering Design 44 (4) (2009) 263–271.
[8] B. Pan, D. Wu, Z. Wang, Y. Xia, High-temperature digital image correlation method for full-field deformation measurement at 1200 c, Measurement science and technology 22 (1) (2010) 015701.
[9] M. D. Novak, F. W. Zok, High-temperature materials testing with full-field strain measurement: experimental design and practice, Review of scientific instruments 82 (11) (2011) 115101.
[10] M. Appleby, D. Zhu, G. Morscher, Mechanical properties and real-time damage evaluations of environmental barrier coated sic/sic cmcs subjected to tensile loading under thermal gradients, Surface and Coatings Technology 284 (2015) 318–326.
[11] T. Archer, P. Beauchene, C. Huchette, F. Hild, Global digital image correlation up to very high temperatures with grey level corrections, Measurement Science and Technology 31 (2) (2019) 024003.
[12] V. Maurel, L. Rémy, M. Harvey, H. T. du Montcel, A. Koster, The respective roles of thermally grown oxide roughness and nial coating anisotropy in oxide spallation, Surface and Coatings Technology 215 (2013) 52–61.
[13] A. Blug, D. J. Regina, S. Eckmann, M. Senn, A. Bertz, D. Carl, C. Eberl, Real-time gpu-based digital image correlation sensor for marker-free strain-controlled fatigue testing, Applied Sciences 9 (10) (2019) 2025.
[14] F. Conrad, A. Blug, J. Kerl, J. Fehrenbach, D. J. Regina, A. Bertz, C. Kontermann, D. Carl, M. Oechsner, Gpu-based digital image correlation system for uniaxial and biaxial crack growth investigations, Procedia Structural Integrity 28 (2020) 2195–2205.
[15] Y. Dong, B. Pan, A review of speckle pattern fabrication and assessment for digital image correlation, Experimental Mechanics 57 (8) (2017) 1161–1181.

[16] N. Guillermin, A. Köster, Technique de suivi par gravure laser pour une mesure de champ de déplacement, brevet INPI n°FR2109996 (2021).
[17] N. Guillermin, Détection et simulation d'instabilités viscoplastiques dans les disques de turbines, Ph.D. thesis, Université Paris sciences et lettres (2022).
[18] T. Hutt, P. Cawley, Feasibility of digital image correlation for detection of cracks at fastener holes, NDT & e International 42 (2) (2009) 141–149.
[19] J. Rupil, S. Roux, F. Hild, L. Vincent, Fatigue microcrack detection with digital image correlation, The Journal of Strain Analysis for Engineering Design 46 (6) (2011) 492–509.
[20] S. Feld-Payet, G. Le Besnerais, V. Bonnand, D. Pacou, L. Thiercelin, Crack path tracking from full field measurements: A novel empirical methodology, Strain 56 (2) (2020) e12333.
[21] Y.-A. Hsieh, Y. J. Tsai, Machine learning for crack detection: Review and model performance comparison, Journal of Computing in Civil Engineering 34 (5) (2020) 04020038.
[22] M. S. Kaseko, S. G. Ritchie, A neural network-based methodology for pavement crack detection and classification, Transportation Research Part C: Emerging Technologies 1 (4) (1993) 275–291.
[23] M. Gavilán, D. Balcones, O. Marcos, D. F. Llorca, M. A. Sotelo, I. Parra, M. Ocaña, P. Aliseda, P. Yarza, A. Amírola, Adaptive road crack detection system by pavement classification, Sensors 11 (10) (2011) 9628–9657.
[24] Y. Shi, L. Cui, Z. Qi, F. Meng, Z. Chen, Automatic road crack detection using random structured forests, IEEE Transactions on Intelligent Transportation Systems 17 (12) (2016) 3434–3445.
[25] E. Charkaluk, A. Bignonnet, A. Constantinescu, K. Dang Van, Fatigue design of structures under thermomechanical loadings, Fatigue & Fracture of Engineering Materials & Structures 25 (12) (2002) 1199–1206.
[26] K. Kim, R. Van Stone, Crack growth under thermo-mechanical and temperature gradient loads, Engineering fracture mechanics 58 (1-2) (1997) 133–147.
[27] R. Duckert, G. Halford, F. Holland, S. Kalluri, F. Ritzert, M. Verrilli, Thermomechanical and bithermal fatigue behavior of cast B1900+ Hf and wrought Haynes 188, ASTM International, 1992.
[28] S. Kalluri, G. R. Halford, Damage mechanisms in bithermal and thermomechanical fatigue of haynes 188, in: Thermomechanical Fatigue Behavior of Materials, Vol. 1186, American Society for Testing and Materials Philadelphia, 1993, pp. 126–143.
[29] V. Maurel, A. Köster, L. Rémy, M. Rambaudon, D. Missoum-Benziane, V. Fontanet, F. Salgado-Goncalves, A. Heudt, H. Wang, M. Trabelsi, Fatigue crack growth under large scale yielding condition: the need of a characteristic length scale, International Journal of Fatigue 102 (2017) 184–201.
[30] V. Maurel, V. Chiaruttini, A. Koster, D. Missoum-Benziane, Fatigue crack growth under large scale yielding condition: a tool based on explicit crack growth, Journal of Theoretical, Computational and Applied Mechanics (2022).
[31] F. Salgado Goncalves, Caractérisation expérimentale et modélisation des interactions entre fissures et perçages multiples à haute température en élastoplasticité généralisée ou confinée, Ph.D. thesis, Paris, ENMP (2013).
[32] M. Trabelsi, Propagation de fissures en fatigue oligocyclique multiaxiale à haute température pour le superalliage haynes® 188, Ph.D. thesis, Paris Sciences et Lettres (ComUE) (2019).
[33] Haynesintl., Haynes international aerospace alloys, http://www.haynesintl.com.
[34] A. Chaieb, N. Mozzani, A. Parrot, A. Ambard, A. Köster, J. Crépin, Anisothermal behaviour of unirradiated cwsr zircaloy-4 fuel clads under ria conditions, TopFuel, Prague (2018).
[35] P. Luo, Y. Chao, M. Sutton, W.-H. Peters, Accurate measurement of three-dimensional deformations in deformable and rigid bodies using computer vision, Experimental mechanics 33 (2) (1993) 123–132.
[36] J.-J. Orteu, 3-d computer vision in experimental mechanics, Optics and lasers in engineering 47 (3-4) (2009) 282–291.
[37] M. A. Sutton, J. J. Orteu, H. Schreier, Image correlation for shape, motion and deformation measurements: basic concepts, theory and applications, Springer Science & Business Media, 2009.
[38] B. Pan, K. Qian, H. Xie, A. Asundi, Two-dimensional digital image correlation for in-plane displacement and strain measurement: a review, Measurement science and technology 20 (6) (2009) 062001.
[39] I. Arganda-Carreras, V. Kaynig, C. Rueden, K. W. Eliceiri, J. Schindelin, A. Cardona, H. Sebastian Seung, Trainable weka segmentation: a machine learning tool for microscopy pixel classification, Bioinformatics 33 (15) (2017) 2424–2426.
[40] T. K. Ho, Random decision forests, in: Proceedings of 3rd international conference on document analysis and recognition, Vol. 1, IEEE, 1995, pp. 278–282.
[41] L. Breiman, Random forests, Machine learning 45 (1) (2001) 5–32.
[42] G. Forman, et al., An extensive empirical study of feature selection metrics for text classification., J. Mach. Learn. Res. 3 (Mar) (2003) 1289–1305.
[43] M. Hossin, M. N. Sulaiman, A review on evaluation metrics for data classification evaluations, International journal of data mining & knowledge management process 5 (2) (2015) 1.
[44] F. Pedregosa, G. Varoquaux, A. Gramfort, V. Michel, B. Thirion, O. Grisel, M. Blondel, P. Prettenhofer, R. Weiss, V. Dubourg, J. Vanderplas, A. Passos, D. Cournapeau, M. Brucher, M. Perrot, E. Duchesnay, Scikit-learn: Machine learning in Python, Journal of Machine Learning Research 12 (2011) 2825–2830.
[45] Zset software, non-linear material and structure analysis suite.
URL http://www.zset-software.com
[46] C. Geuzaine, J.-F. Remacle, Gmsh: A 3-d finite element mesh generator with built-in pre-and post-processing facilities, International journal for numerical methods in engineering 79 (11) (2009) 1309–1331.
[47] D. S., Identification d'une loi de comportement à 7 paramètres avec double viscosité sur le superalliage à base cobalt haynes 188, Note technique Snecma (1999).
[48] J.-L. Chaboche, A. Gaubert, P. Kanouté, A. Longuet, F. Azzouz, M. Mazière, Viscoplastic constitutive equations of combustion chamber materials including cyclic hardening and dynamic strain aging, International journal of plasticity 46 (2013) 1–22.

[49] H. E. Chaieb, Study of a near-eutectic zinc-aluminum coating deposited on steel by hot-dip galvanization: microstructural aspects, crystallographic texture and deformation and damage mechanisms, in: Thermomechanics of Materials Seminar at Centre des Matériaux des MINES ParisTech, 2021.
[50] M. Kamaya, Low-cycle fatigue crack growth prediction by strain intensity factor, International Journal of Fatigue 72 (2015) 80–89.
[51] P. Cussac, C. Gardin, V. Pelosin, G. Hénaff, L. de Baglion, O. Ancelet, S. Courtin, Low-cycle fatigue crack initiation and propagation from controlled surface imperfections in nuclear steels, International Journal of Fatigue 139 (2020) 105703.
[52] V. Maurel, L. Rémy, F. Dahmen, N. Haddar, An engineering model for low cycle fatigue life based on a partition of energy and micro-crack growth, International Journal of Fatigue 31 (5) (2009) 952–961.
[53] N. Guillermin, J. Besson, A. Köster, L. Lacourt, M. Mazière, H. Chalons, S. Forest, Experimental and numerical analysis of the portevin-le chatelier effect in a nickel-base superalloy for turbine disks application, International Journal of Solids and Structures (2022) 112076.
[54] Y. Wang, A. Charbal, F. Hild, S. Roux, L. Vincent, Crack initiation and propagation under thermal fatigue of austenitic stainless steel, International Journal of Fatigue 124 (2019) 149–166.
[55] F. Mauget, F. Hamon, M. Morisset, J. Cormier, F. Riallant, J. Mendez, Damage mechanisms in an eb-pvd thermal barrier coating system during tmf and tgmf testing conditions under combustion environment, International Journal of Fatigue 99 (2017) 225–234.
[56] M. Böcker, H. R. Babu, S. Henkel, M. Raddatz, U. Gampe, H. Biermann, Planar-biaxial thermo-mechanical fatigue behavior of nickel-base superalloy inconel 718 under proportional loading, Metallurgical and Materials Transactions A (2022) 1–14.
[57] T. Nicholas, M. L. Heil, G. K. Haritos, Predicting crack growth under thermo-mechanical cycling, International Journal of Fracture 41 (3) (1989) 157–176.
[58] C. J. Pretty, M. T. Whittaker, S. J. Williams, Crack growth of a polycrystalline nickel alloy under tmf loading, in: Advanced Materials Research, Vol. 891, Trans Tech Publ, 2014, pp. 1302–1307.
[59] P. J. Bonacuse, S. Kalluri, Axial-torsional, thermomechanical fatigue behavior of haynes 188 superalloy, in: AGARD CONFERENCE PROCEEDINGS AGARD CP, AGARD, 1996, pp. 15–10.